Journal of ELECTRONIC MATERIALS, Vol. 49, No. 10, 2020
https://doi.org/10.1007/s11664-020-08334-0

Impedance Spectroscopy and Photovoltaic Effect of Oxygen Defect Engineering on $KNbO_3$ Ferroelectric Semiconductors

FEI HAN,[1] YUJIE ZHANG,[1] CHANGLAI YUAN,[1,2,4,5] XIAO LIU,[1] BAOHUA ZHU,[1,2,6] FEI LIU,[1] LIUFANG MENG,[1] JIANG WANG,[1] CHANGRONG ZHOU,[1,2] and GUANGHUI RAO[1,2,3,7]

1.—College of Material Science and Engineering, Guilin University of Electronic Technology, Guilin 541004, People's Republic of China. 2.—Guangxi Key Laboratory of Information Materials, Guilin University of Electronic Technology, Guilin 541004, People's Republic of China. 3.—Institute of Physics, Chinese Academy of Sciences, Beijing 100190, People's Republic of China. 4.—e-mail: yclai-2002@163.com. 5.—e-mail: yclguet@yahoo.com. 6.—e-mail: uestczrk@126.com. 7.—e-mail: rgh@guet.edu.cn

Perovskite-oxide $(1-x)KNbO_3$-$xBaCo_{1/2}Nb_{1/2}O_{3-\delta}$ (KN-BCN; x = 0.00–0.20) ferroelectric semiconductor ceramics with oxygen defects are successfully prepared via a conventional solid-state sintering method. X-ray diffraction data indicate that the crystal symmetry evolves from orthogonal to tetragonal at increasing x values. Raman spectroscopic analysis confirms the long-range polarization of all compositions. X-ray photoelectron spectroscopy shows that the detailed chemical formula of 0.90KN-0.10BCN ceramics is $0.90KNbO_3$-$0.10BaCo_{1/2}Nb_{1/2}O_{2.90}$. Room-temperature ferroelectricity weakens when the x value increases. The optical band gap narrows from 3.25 eV for x = 0.00 to 1.57 eV for x = 0.20, and the minimum value of $\sim$ 1.28 eV occurs in the 0.90KN-0.10BCN ceramic. Impedance analysis illustrates that the conduction mechanism of grains is mainly internal electron conduction, and that of the grain boundary is intrinsic conduction. The conducting mechanism of the ceramic system follows ohmic behavior by log I–log U curves. The maximum short-circuit photocurrent density and open-circuit photovoltage are 6.68 nA cm^{-2} and 0.80 V, and stable output is maintained. The KN-BCN ceramic system can be used in photovoltaic materials.

Key words: Perovskites, band gap, ferroelectric semiconductors, impedance spectroscopy

INTRODUCTION

ABO_3-type perovskite oxides have attracted interest because of their optical properties that are essential to photocatalysis, photovoltaics, and solar cells.[1–5] Ferroelectric semiconductor perovskite materials have been widely studied as candidate optoelectronic materials. As an excellent photoresponsive material, a ferroelectric internal electric field is expected to greatly improve the separation of electron–hole pairs and efficiency.[6] However, most ferroelectrics exhibit optical band gaps that are usually larger than 3 eV and only absorb in the ultraviolet range. Therefore, effective methods for regulating band gaps are urgently needed. At present, halides and oxides in perovskite structural materials have attracted considerable attention. However, perovskite halides are extremely sensitive to the effects of temperature and humidity and are very unstable. Perovskite ferroelectric semiconductor oxides, such as $BiFeO_3$,[7–10] $Pb(Zr_{0.5}Ti_{0.5})O_3$,[11–13] and $KNbO_3$,[14–16] are widely used in photovoltaic and photocatalytic applications. The band gap of $Pb(Zr_{0.5}Ti_{0.5})O_3$ is $>$ 3.6 eV, and the corresponding absorption of the semiconductor can only use less than 8% of the solar spectrum. $BiFeO_3$ thin films

(Received February 5, 2020; accepted July 14, 2020; published online August 10, 2020)

with room-temperature ferroelectricity have a relatively small optical band gap (approximately 2.4 eV), but their solar absorption efficiency is only about 15%. $KNbO_3$ has attracted increasing attention because of its low optical band gap and high absorbability.

The band gap engineering of $KNbO_3$ ceramics has been the focus of many researchers. The band gap of ceramics was recently decreased to 1.18 eV, which is considerably smaller than that of $KNbO_3$ ($\sim$ 3.2 eV), when $(1-x)KNbO_3$-$xBaNi_{1/2}Nb_{1/2}O_{3-\delta}$ is used.[14] The maximum value of the valence band is dominated by hybrid Ni 3*d* and O 2*p* states, whereas the conduction band is minimally composed of a Nb 4*d* state. Ni 3*d* plays a vital role in the reduction of the band gaps of ceramics. The band gap of a ceramic can be decreased from 3.25 eV to 2.25 eV by using $KNbO_3$ with $BiFeO_3$ compared with pure $KNbO_3$.[17] The increase in the valence band value may be due to the substitution of Nb^{5+} with Fe^{3+} and the subsequent enhanced repulsion between O 2*p* and Fe 3*d* states. The optical band gap of $KNbO_3$ can be reduced to 2.89 eV by doping with Ba^{2+}/Bi^{3+} and Zn^{2+} ions at A and B sites, respectively.[18]

In this work, the solid–solution ceramics of $(1-x)KNbO_3$-$xBaCo_{1/2}Nb_{1/2}O_{3-\delta}$ (x = 0, 0.02, 0.05, 0.10, 0.20) are investigated by solid-state methods. The structures, lattice vibrations, optical properties, impedance spectroscopy, dielectric/ferroelectric properties, and photoresponse of the ceramics are systematically investigated. Low band gap, satisfactory room-temperature ferroelectricity, and high photocurrent density of $\sim$ 6.68 nA cm^{-2} are obtained in the system. This research is of great significance for understanding the band gap engineering and ferroelectric properties of perovskite $KNbO_3$ materials, and provides alternatives for oxide ferroelectric photovoltaic devices.

EXPERIMENTAL

All the reagents used were of analytical pure grade. K_2CO_3 (99.0%), Nb_2O_5 (99.9%), $BaCO_3$ (99.0%), and Co_2O_3 (99.0%) were used as starting reagent materials. The raw materials, with a chemical formula of $(1-x)KNbO_3$-$xBaCo_{1/2}Nb_{1/2}O_{3-\delta}$ (x = 0.00, 0.02, 0.05, 0.10, 0.20), were milled with a ZrO_2 ball for 24 h in anhydrous ethanol medium. The dried slurries were calcined in air at 900°C for 12 h. The calcined powder was added with polyvinyl alcohol (PVA, 5 wt.%), dried, and ground. The powder was then pressed into a cylindrical disc with 12 mm diameter and 0.6 mm thickness at 120 MPa. For the removal of PVA, the ceramic samples were heated to 600°C for 2 h. Finally, the samples were sintered at 1050–1120°C for 3 h in air. For the analysis of electrical properties, an Ag paste was printed on a screen, polished with sandpaper on both sides of the ceramics, and fired at 580°C for 30 min.

The structure and composition of the samples were analyzed by an x-ray diffraction (XRD) system (PIXCED3D, Netherlands) using Cu-K_α radiation with 2θ ranging from 20° to 80°. Lattice vibration was studied by Raman spectroscopy (LabRAM HR Evolution, HORIBA France). An ultraviolet–visible–near infrared spectrophotometer (Lambda750, PerkinElmer, USA) with an integrated sphere was used for optical absorption tests. X-ray photoelectron spectroscopy (XPS, XSAM-800) was used for analysis of the chemical valence changes and polarization intensity (P) under an electric field (E) with a ferroelectric testing system (TF Analyzer 2000 HS, Germany). Variable temperature impedance was measured with a precision impedance analyzer (Agilent 4294A, USA). The frequency and temperature of the impedance were measured at 40 Hz to 1 MHz and 330–420°C, respectively. The impedance data were fitted using ZView 2 software. Light was provided by xenon lamps with standard solar energy (AM1.5), and the photovoltaic effect was obtained from a Keithley 2410 digital source meter.

RESULTS AND DISCUSSION

Figure 1a shows the XRD patterns of $(1-x)KN$-$xBCN$ (x = 0.00, 0.02, 0.05, 0.10, 0.20) ceramics in the 2θ range of 20°–80°. All the samples exhibit a single perovskite structure, and no secondary phase is present. These results indicate the formation of ceramic solid solutions in the system. Pure KN is an orthorhombic system with a space group of Amm2.[19] Figure 1b shows that the pure KN has typical split peaks of (022) and (200), but only a single peak (020) is seen in doped BCN ceramics. This finding indicates the transition from the orthorhombic phase (Amm2) to tetragonal phase (P4mm). The characteristic peak (020) shifts to lower 2θ angles, indicating an increase in the unit cell size with increasing x. This finding supports the introduction

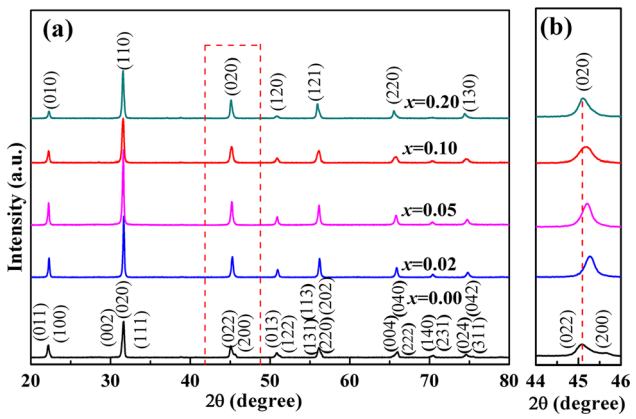

Fig. 1. (a) XRD patterns of KN-BCN ceramics with different x values. (b) Magnified XRD patterns at 2θ = 44°–46°.

of Co^{3+} ions because the ionic radius of Nb^{5+} [$r(Nb^{5+})$ = 0.64 Å)] is smaller than that of Co^{3+} [$r(Co^{3+})$ = 0.68 Å], resulting in lattice expansion.

Through the refinement of $(1 - x)$KN-xBCN with x = 0.00–0.10, the structure is confirmed as orthorhombic (Amm2) with χ^2 values of 3.62, 3.45, 3.11, and 3.27. The XRD peaks of 0.80KN-0.20BCN best fitted by Amm2 with χ^2 value of ~ 2.90 are shown in Fig. 2. The cell parameters (a, b, and c) increase with BCN content because the radius of the Co^{3+} ion is larger than that of the Nb^{5+} ion. This occurrence also causes an increase in cell volume (V). Table I provides the detailed parameters of Rietveld analysis.

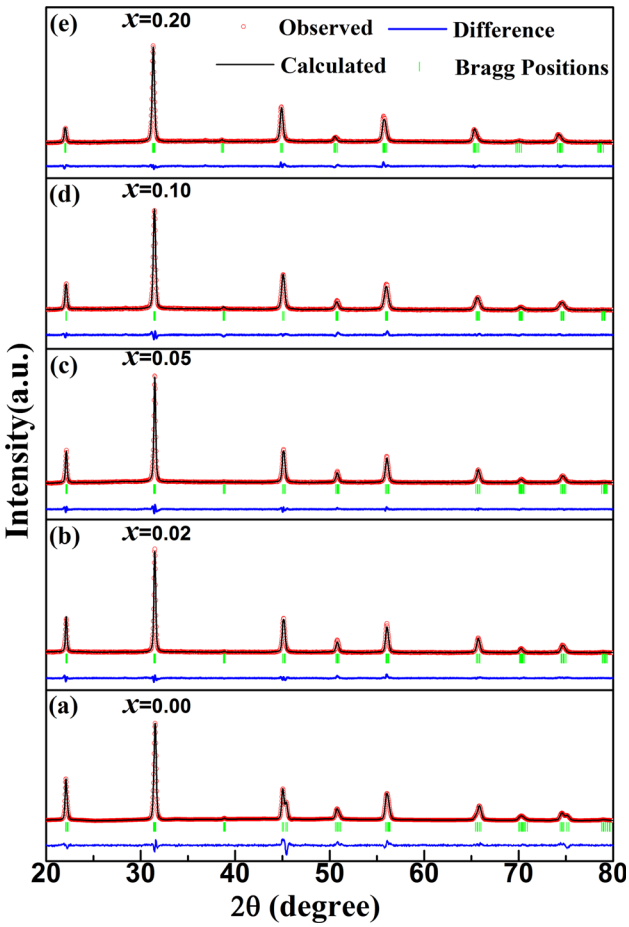

Fig. 2. Refined XRD profiles and crystal structures for KN-BCN ceramics with different x values: (a) x = 0.00, (b) x = 0.02, (c) x = 0.05, (d) x = 0.10, and (e) x = 0.20.

The SEM images of $(1 - x)$KN-xBCN (x = 0.00, 0.02, 0.05, 0.10, 0.20) ceramics are shown in Fig. 3. In Fig. 3a, the surface crystallinity of KN ceramics is good, and the arrangement of compact particles is clear. Figure 3b–e shows the microstructure of BCN-doped samples. The grain size of the samples is not uneven, which may be due to the increase in Co^{3+} at the grain boundary, thereby hindering the movement of the grain boundary and inhibiting the growth of local grains, resulting in a significant difference in grain size.[20] In addition, obvious pores are formed in the sintering process of KN-BCN ceramics. The increasing number of holes will seriously affect the dielectric loss of the ceramics, which will be confirmed in later dielectric measurements.

Raman spectroscopy is a reliable technique used to determine non-centrosymmetric polar characteristics and crystal structures in advanced functional materials. This technique is more sensitive to local lattice vibrations compared with XRD.[21] The Raman spectra of $(1 - x)$KN-xBCN (x = 0.00, 0.02, 0.05, 0.10, 0.20) ceramics are presented in Fig. 4. The modes of Raman spectroscopy are demonstrated in the literature for determining single-crystal distribution principle for KN.[22] The Raman spectrum shows that KN has an orthogonal crystal symmetry and long-range polarity sequence. The Raman peaks at 192 and 833 cm^{-1}, are considered ferroelectric long-range orders in solid solutions based on KN.[23] The peak centered at 272 cm^{-1} shifts to a lower wavenumber, and a smaller peak appears at 295 cm^{-1}, which are consistent with the orthogonal–tetragonal phase transition.[24] As the dopant increases, the 833 cm^{-1} bond shifts to the left, indicating that the Co-O bond strength increases significantly.

Table I. Refined structural parameters for $(1 - x)$KN-xBCN ceramics with different x values

Parameters Space group	x = 0.00 Amm2	x = 0.02 P4mm	x = 0.05 P4mm	x = 0.10 P4mm	x = 0.20 P4mm
a (Å)	3.9934	4.0092	4.0098	4.0215	4.0431
b (Å)	5.6814	5.6820	5.6884	5.6947	5.7179
c (Å)	5.7006	5.6970	5.6935	5.6822	5.6869
c/a	1.4275	1.4210	1.4199	1.4130	1.4066
V (Å^3)	129.33	129.78	129.86	130.13	131.47
Rp	23.7	22.3	16.8	17.6	19.3
Rwp	12.5	11.5	9.91	11.4	11.1
Rexp	6.41	6.21	5.62	6.29	6.54
χ^2	3.62	3.45	3.11	3.27	2.90

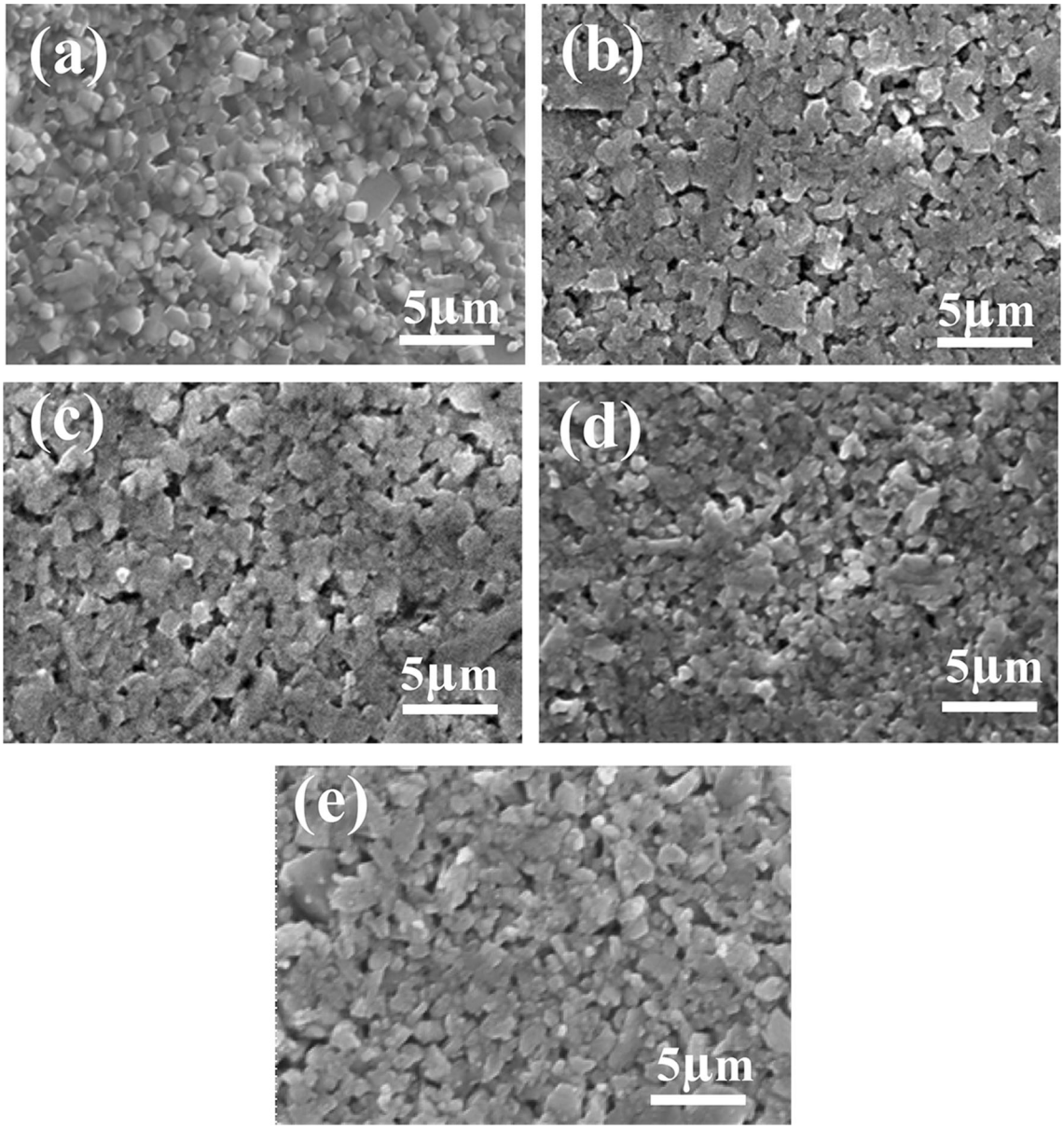

Fig. 3. SEM images of KN-BCN ceramics with different x values: (a) x = 0.00, (b) x = 0.02, (c) x =0.05, (d) x = 0.10, and (e) x = 0.20.

XPS is often used to analyze chemical composition and atomic valence states on the surface of materials. Figure 5a shows the full XPS spectra of KN and 0.90KN-0.10BCN ceramics. Except for Ba and Co, the peaks of the detected elements are similar. The C 1*s* peak at 284.6 eV is usually used as a reference standard.[25] In Fig. 5b, the K $2p_{3/2}$ and K $2p_{1/2}$ binding energies are 291.68 and 294.28 eV, respectively, indicating that the spin–orbit splitting energy is 2.6 eV; hence, the +1 valence is proven to be the effective charge of K ions.[26,27] Figure 5c shows that the spin–orbital splits of the Co $2p_{3/2}$ and Co $2p_{1/2}$ peaks are located at 779.68 and 795.18 eV, respectively, which are consistent with the binding energies of Co_2O_3 and $Co(OH)_2$, respectively.[28] As shown in Fig. 5d, the peak of Ba $3d_{5/2}$ is 779.68 eV, which is close to the previously reported Ba^{2+} oxide.[29] In Fig. 5e, the binding energies of Nb $3d_{5/2}$ and Nb $3d_{3/2}$ are located at 206.78 and 209.48 eV, respectively, corresponding to the values reported in KN.[30] Figure 5f shows the lattice oxygen peaks of 529.78 and 531.78 eV in the fitted O 1*s* spectrum, demonstrating the presence of OH groups on the surface of KN-BCN. These data are consistent with a previous report.[31] According to the above results, the detailed chemical formula of 0.90KN-0.10BCN

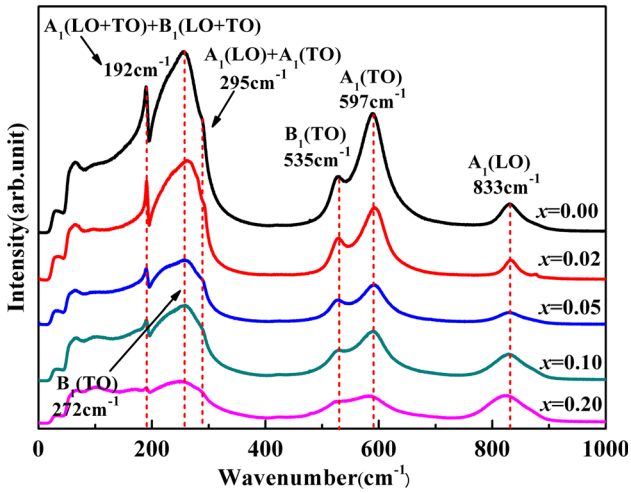

Fig. 4. Raman spectra of KN-BCN ceramics with different x values.

is determined to be $0.90KNbO_3$-$0.10BaCo_{1/2}Nb_{1/2}O_{2.90}$.[32]

Figure 6 displays the relative permittivity (ε_r) and dielectric loss ($\tan\delta$) for $(1-x)KNbO_3$-$xBaCo_{1/2}Nb_{1/2}O_{3-\delta}$ ceramics measured at 150 kHz. KN exhibits two peaks, namely, the ferroelectric orthorhombic to ferroelectric tetragonal ($O \rightarrow$ T) transition peak at 245°C and the tetragonal to paraelectric cubic ($T \rightarrow$ C) transition peak at 408°C, also known as Curie temperature (T_c).[33] By doping BCN content of x = 0.02 to x = 0.10, two transition peaks similar to KN are found at ~ 248°C and ~ 395°C, respectively. However, for x = 0.20, the transitional peak almost disappears, indicating the occurrence of a cubic or pseudocubic phase. The relative permittivity of all the doping ceramics decreases with increasing doping content at the phase transition point. This decrease indicates the weakening of the polarization order. The $\tan\delta$ increases with increasing x, indicating that the quality of the ceramics is reduced by the doping of BCN.

The P–E hysteresis loops of $(1-x)$KN-xBCN (x = 0.00, 0.02, 0.05, 0.10, 0.20) ceramics measured under an electric field of 30 kV cm^{-1} are shown in Fig. 7. The P–E hysteresis loop for pure KN has a polarization of 5.26 μC cm^{-2}. Within the range of x = 0.02–0.20, the polarization decreases to 3.49, 2.97, 1.33, and 0.75 μC cm^{-2}. The remnant polarization intensity with x values decreases mainly due to the structural phase transition from ferroelectric to paraelectric.[34] Oxygen vacancy contributes to the behavior, resulting in difficulty of domain-wall and domain inversion with increasing BCN content.[35] Nb^{+5} is replaced with Co^{+3}, causing long-range ordered displacement of Nb^{+5} and structural local strain. Given the electronegativity of Ba and K, the ionic strength of the modified A-O bond is partly replaced with Ba^{+2} at the A-site.

Figure 8a shows the absorption spectra of KN-BCN ceramics. The absorption range of KN-BCN is far wider than that of pure KN in the ultraviolet, visible, and infrared regions, showing excellent absorption characteristics. In Fig. 8b, the optical band gap is obtained by the tangential intercept in the curve of the Kubelka–Munk function $(\alpha h\nu)^2$ versus $h\nu$ for the direct-band-gap materials, where α is the absorbance and $h\nu$ is the photon energy.[36] The colors of the samples (inset of Fig. 8b) change from white to blue and finally to black, indicating the reduction in the band gap. With increasing BCN content, the band gap of KN-BCN is in the range of 1.28–1.67 eV, which is considerably smaller than that of pure KN (~ 3.22 eV). The band gap reaches a minimum value of 1.28 eV for x = 0.10. The excitation of the band gap is caused by the doping of Co^{3+} ions, which transfers the charge of hybrid Co 3d and O 2p to the Nb 4d state. The reduction in the band gap of KN-BCN lays the foundation for photovoltaic and photocatalytic applications.

Figure 9 shows the impedance complex plane of 0.90KN-0.10BCN ceramics measured at 330–420°C for air [(a)–(b)] and N_2 [(c)–(d)]. The illustration of Fig. 9a is an equivalent circuit. A perfect fit can be achieved through the combination of R, C, and CPE.[37] The radius of the curve decreases with increasing temperature in Fig. 9a and b, indicating the reduced resistance of grains and grain boundaries. This finding is due to the decrease in the barrier height at high temperature and the increase in the charge mobility and conductivity of the sample because electrons can easily break away from the nucleus.[38] Figure 9c and d shows the measurement under N_2, and its trend is basically the same as that in the air. However, the resistance of grain and grain boundary is higher than that of air, because oxygen absorption reaction can occur when the sample contacts in air.[39]

The impedance fit residuals are shown in Fig. 10-a. The fitting error of air and N_2 at 420°C ranges from −0.001 to +0.006. These results show that the circuit is suitable for fitting, and the error is small. The fit accurately represents electrical microregions inside the ceramic body. Figure 10b shows an Arrhenius diagram of grain and grain boundary conductance for the 0.90KN-0.10BCN ceramic in air and N_2. The activation energy (E_a) represents the ease of ion hopping and is related to the crystal structure and, in particular, to the openness of the conduction pathways.[40] In air and N_2, the E_a values of particles are 0.61 and 0.58 eV, respectively, which are about half of the optical band gap (1.28 eV), indicating that the conduction mechanism is mainly internal electron conduction.[41] The E_a values of grain boundary in air and N_2 are 0.73

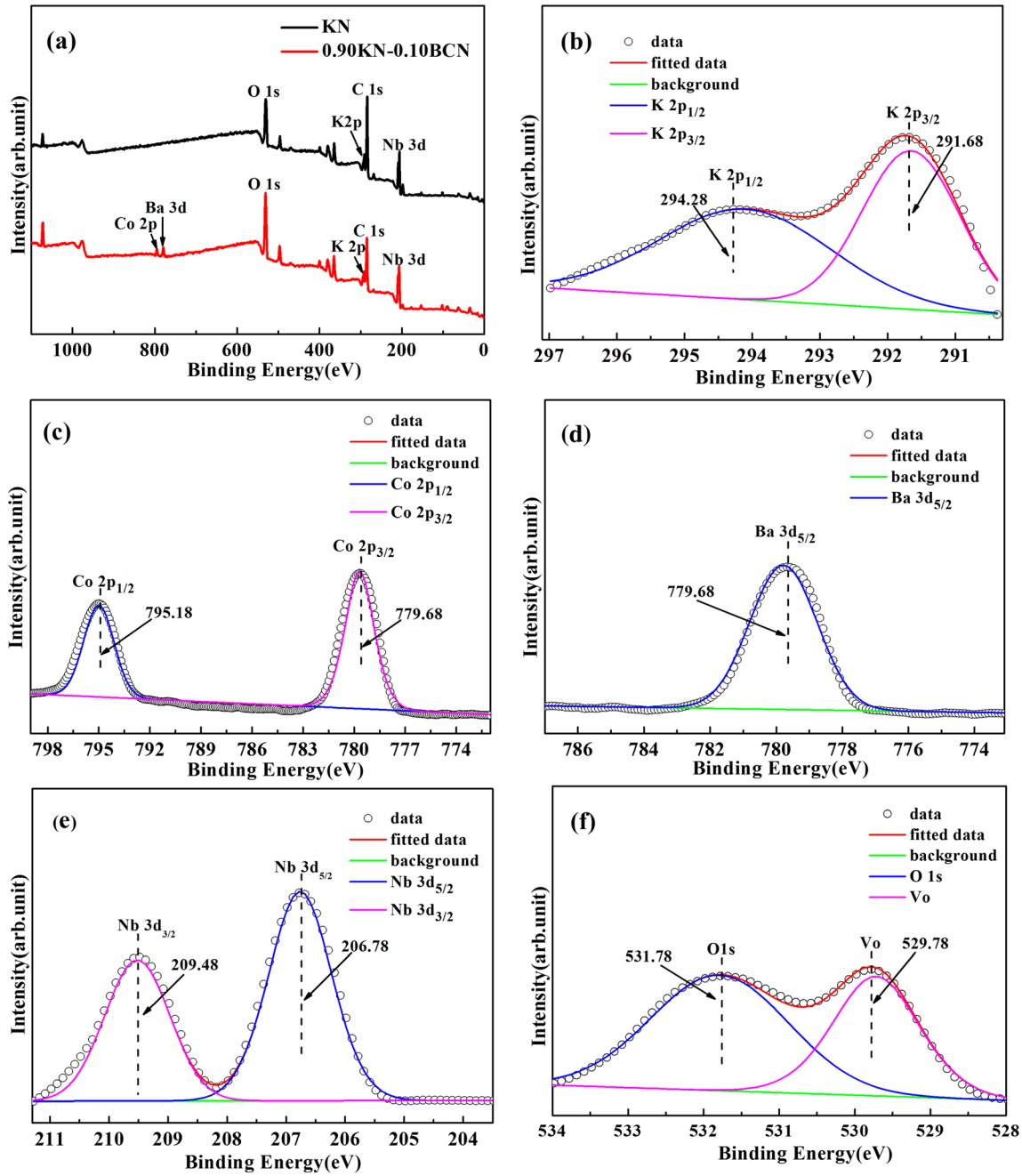

Fig. 5. (a) XPS spectra of KN and 0.90KN-0.10BCN ceramics and high-resolution XPS spectra of (b) K 2*p*, (c) Co 2*p*, (d) Ba 3*d*, (e) Nb 3*d*, and (f) O 1*s*.

and 0.71 eV, respectively, which belong to the intrinsic conductive mechanism.[42] The grain and grain boundary conductivity of N_2 samples is lower than that of air samples, suggesting a *p*-type conduction behavior for grain and grain boundary regions. This finding is consistent with the *p*-type behavior commonly observed in Co oxide or Co-containing oxides.[40,43]

Figure 11 shows the Cole–Cole plots of 0.9KN-0.1BCN ceramic under different DC biases in air. The electrical behavior of decreasing resistivity with increasing DC bias denotes that the sample shows typical *p*-type conduction, which is consistent with the literature.[44] The illustration in Fig. 11 shows the log *I*–log *U* curve of 0.9KN-0.1BCN ceramics. Information on the conduction mechanism can be determined using the slope of the log *I*–log *U*

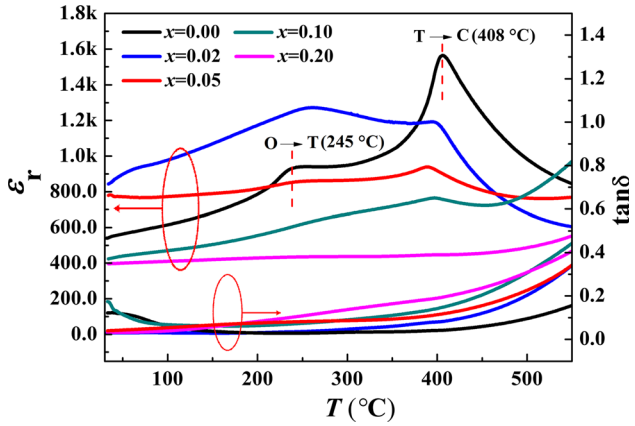

Fig. 6. Temperature dependence of ε_r and tanδ of KN-BCN ceramics with different x values at 150 kHz.

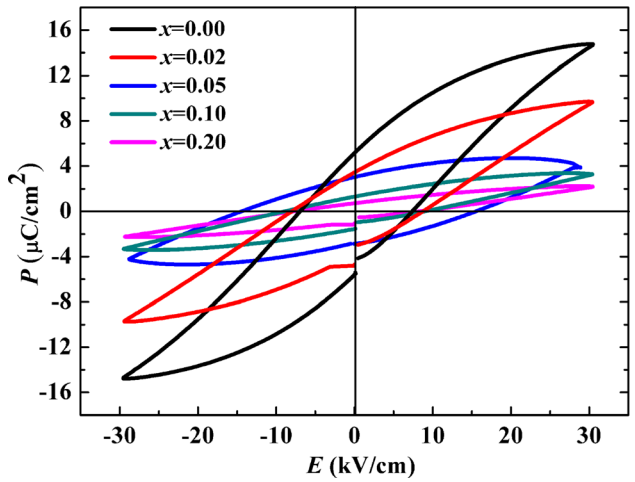

Fig. 7. P–E hysteresis loops of KN-BCN ceramics with different x values.

curve.[45] The linear behavior for the log I–log U curve can also be observed with DC bias ranging from 4 V to 14 V, and the slope of all the electrical components is fitted to $\sim$ 1 in air. Understandably, the conduction mechanisms of all electrical microregions follow the ohmic behavior.

Given the above findings, the x = 0.10 ceramics have relatively higher residual polarization and smaller band gap. Hence, the photocurrent of the x = 0.10 ceramics is measured, and the corresponding results are demonstrated in Fig. 12a. An ITO film with thickness of $\sim$ 300 μm was used as electrode, and 100 mW cm^{-2} simulated AM 1.5 sunlight was provided to the sample by a xenon lamp. The samples were polarized at room temperature with 20 kV cm^{-1} electric field for 10 min. The short-circuit photocurrent density (J_{sc}) and open-circuit photovoltage (V_{oc}) measured under light are 1.36 nA cm^{-2} and 0.36 V, respectively, and the influence of the dark environment is negligible. The positive polarizations J_{sc} and V_{oc} are 6.68 nA cm^{-2} and 0.80 V, respectively, whereas those on the negative polarizations are 2.71 nA cm^{-2} and 0.66 V, respectively. The effect of positive polarization is obviously greater than that of negative polarization. This finding confirms the existence of the ferroelectric photovoltaic effect. Figure 12b shows the simulation of the typical conversion of light and the dark photocurrent densities of the x = 0.10 samples. The photocurrent density of stable and significant response can be detected by turning on/off the lamp. The findings indicate that the photocurrent can be steadily produced under the action of light. The photoresponse indicates that KN-BCN has potential application in the photovoltaic field.

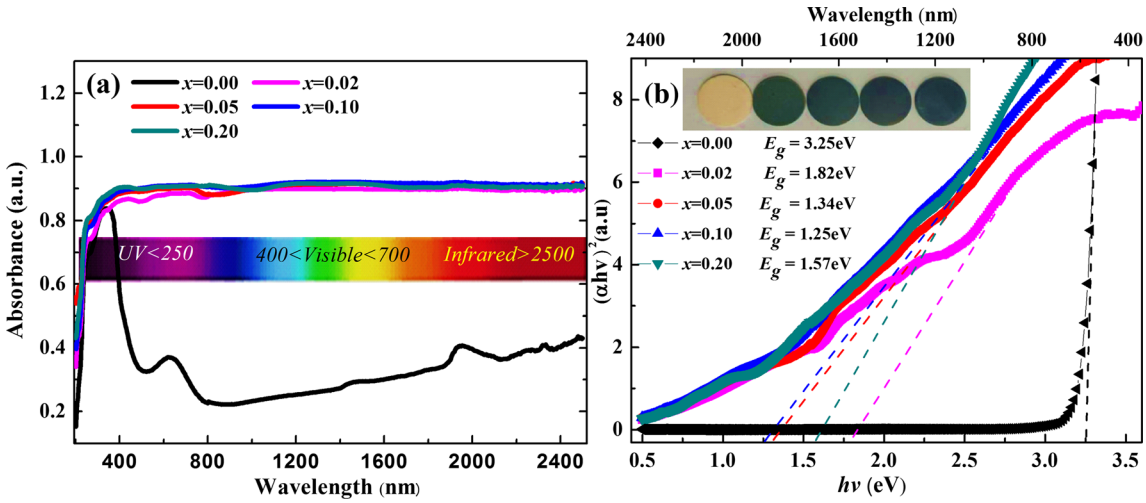

Fig. 8. (a) Absorption spectra of KN-BCN ($0 \le x \le 0.2$) ceramics. (b) Tauc plots of optical band gaps for KN-BCN ceramics with different x values. The illustration is a physical picture of the sample.

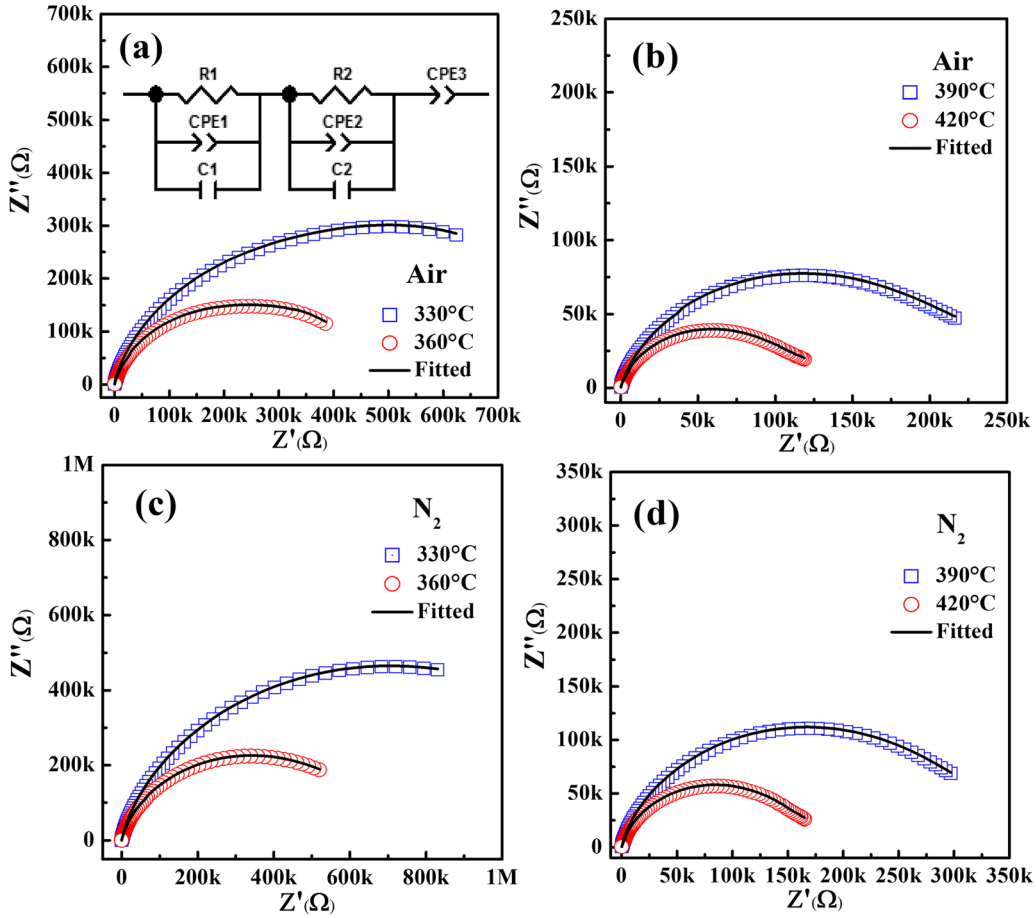

Fig. 9. Impedance complex planes and fitted simulations of 0.90KN-0.10BCN ceramic measured at temperatures of 360–420°C under air (a)–(b) and N_2 (c)–(d).

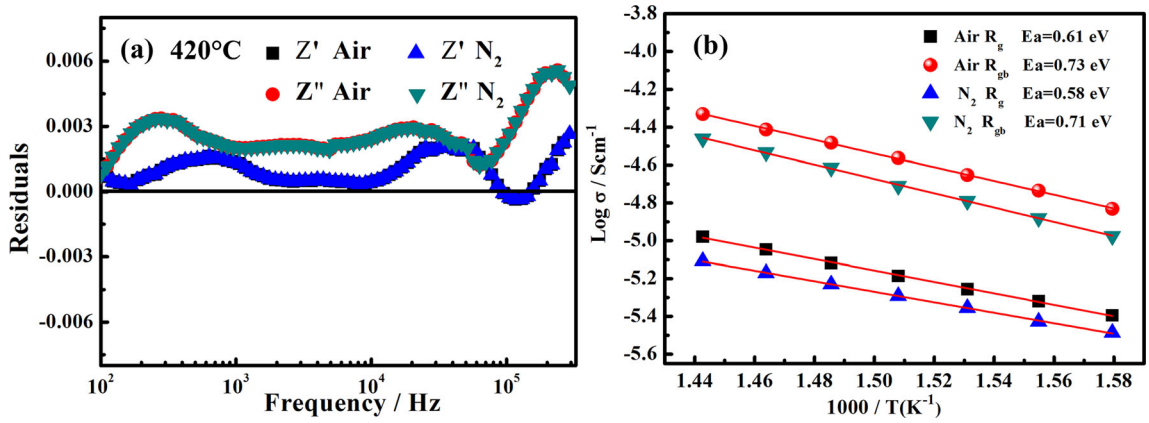

Fig. 10. (a) *Z′*, *Z″* versus frequency residuals under air and N_2 at 420°C. (b) Arrhenius-type temperature dependence of grain and grain boundary conductivity for 0.90KN-0.10BCN ceramic under different atmospheres.

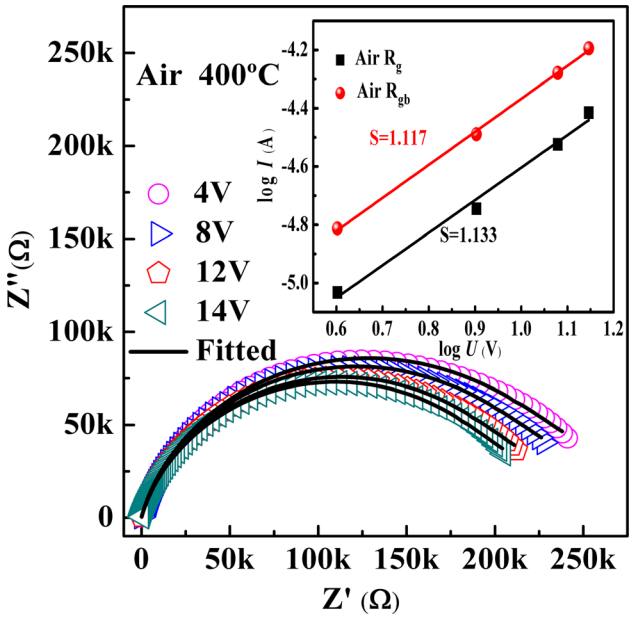

Fig. 11. Cole–Cole plots of 0.90KN-0.10BCN ceramic under different DC biases at 420°C in air. The inset shows the Log *I*–Log *U* curves of R_g and the R_{gb}.

CONCLUSIONS

The structures, optical absorption, impedance spectra, dielectric/ferroelectric properties and photocurrent densities of $(1-x)KNbO_3$-$xBaCo_{1/2}Nb_{1/2}O_{3-\delta}$ (x = 0.00, 0.02, 0.05, 0.10, 0.20) ceramics are investigated. A pure perovskite structure is observed by doping with BCN. Raman spectra confirm the transformation of the phase structure and the weakening of the ferroelectric long-range order. The detailed formula for 0.90KN-0.10BCN ceramic is determined to be $0.90KNbO_3$-$0.10BaCo_{1/2}Nb_{1/2}O_{2.90}$ by XPS analysis. The optical band gap of the 0.90KN-0.10BCN ceramics is 1.25 eV, which is 61.5% less than that of pure KN. The short-circuit photocurrent density and open-circuit photovoltage are 6.68 nA cm^{-2} and 0.80 V, respectively. Therefore, BCN doping can reduce the band gap, rendering the ceramic a potential candidate for photovoltaic applications. In air and N_2, the conduction mechanism of grain and grain boundary are internal electron conduction and intrinsic conduction, respectively. The Log *I*–Log *U* curves reveal that the grains and grain boundaries of the samples follow ohmic behavior. These results are helpful for understanding the photoresponse, microstructures and electrical structures of perovskite–oxide ferroelectric semiconductor ceramics.

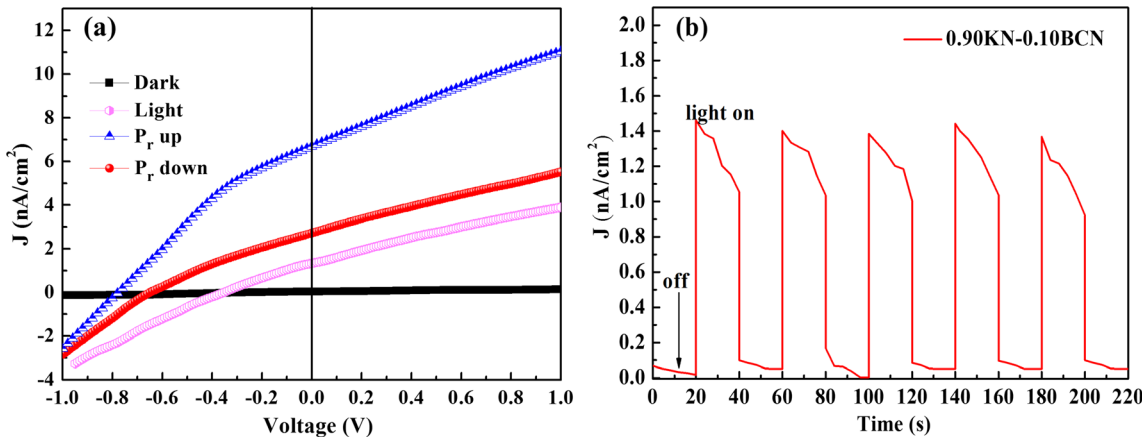

Fig. 12. Photocurrent measurements for the selected polished 0.90KN-0.10BCN samples: (a) photocurrent density (*J*)–voltage (*V*) curves under simulated AM 1.5 sunlight of 100 mW cm^{-2} irradiance and in the dark; the photocurrent densities after positive and negative polarizations are indicated in blue and red, respectively. (b) Simulation of a typical photocurrent density and dark current density conversion (Color figure online).

ACKNOWLEDGMENTS

This work was supported by the National Natural Science Foundation of China (Grant No. 11464006) and Guangxi Key Laboratory of Information Materials (Grant No. 191026–Z).

CONFLICT OF INTEREST

The authors confirm that this manuscript is their original work, and the article was written by the stated authors, who are all aware of its content and approve its submission. The article has not been published previously and is not under consideration for publication elsewhere. No conflict of interest exists. The article will not be published elsewhere in the same form, in any language, without the written consent of the publisher.

REFERENCES

1. S.Y. Yang, J. Seidel, S.J. Byrnes, P. Shafer, C.-H. Yang, M.D. Rossell, P. Yu, Y.-H. Chu, J.F. Scott, and J.W. Ager, *Nat. Nanotechnol.* 5, 143 (2010).
2. M. Alexe and D. Hesse, *Nat. Commun.* 2, 256 (2011).
3. W.S. Choi, M.F. Chisholm, D.J. Singh, T. Choi, G.E. Jellison Jr, and H.N. Lee, *Nat. Commun.* 3, 689 (2012).
4. J. Kreisel, M. Alexe, and P.A. Thomas, *Nat. Mater.* 11, 260 (2012).
5. B. Song, X. Wang, C. Xin, L. Zhang, B. Song, Y. Zhang, Y. Wang, J. Wang, Z. Liu, and Y. Sui, *J. Alloys Compd.* 703, 67 (2017).
6. S.M. Young and A.M. Rappe, *Phys. Rev. Lett.* 109, 116601 (2012).
7. J. Wang, J.B. Neaton, H. Zheng, V. Nagarajan, S.B. Ogale, B. Liu, D. Viehland, V. Vaithyanathan, D.G. Schlom, and U.V. Waghmare, *Cheminform* 299, 1719 (2003).
8. S. Yang, G.B. Ma, L. Xu, C.Y. Deng, and X. Wang, *RSC Adv.* 9, 29238 (2019).
9. Q. Hang, W. Zhou, X. Zhu, J. Zhu, Z.G. Liu, and T. Al-Kassab, *J. Adv. Ceram.* 2, 252 (2013).
10. J. Wu, *Springer* 7, 379 (2018).
11. C.H. Nam, H.-Y. Park, I.-T. Seo, J.-H. Choi, S. Nahm, and H.-G. Lee, *J. Alloys Compd.* 509, 3686 (2011).
12. B. Sahoo and P.K. Panda, *J. Adv. Ceram.* 2, 37 (2013).
13. M. Okayasu and K. Watanabe, *J. Adv. Ceram.* 5, 35 (2016).
14. G. Ilya, W.D. Vincent, T. Maria, G. Gaoyang, D.M. Stein, W. Liyan, C. Guannan, E.M. Gallo, A.R. Akbashev, and P.K. Davies, *Nature* 503, 509 (2013).
15. C.G. Duan, W.N. Mei, J.J. Liu, J.R. Hardy, M.J. Bai, and S. Ducharme, *J. Phys. Condens. Matter* 13, 8189 (2001).
16. X. Lv, Z. Li, J. Wu, D. Xiao, and J. Zhu, *ACS Appl. Mater. Interfaces* 44, 30304 (2016).
17. C. Pascualgonzalez, G. Schileo, and A. Feteira, *Phys. Rev. Lett.* 109, 495902 (2016).
18. F. Wang, I. Grinberg, and A.M. Rappe, *Phys. Rev. B* 89, 5105 (2014).
19. Y. Jiang, Z. Zou, and J. Ye, *J. Mater. Sci.* 41, 1131 (2006).
20. M.A. Mohiddon and K.L. Yadav, *J. Phys. D Appl. Phys.* 40, 7540 (2007).
21. T. Zhang, K. Zhao, J. Yu, J. Jin, Y. Qi, H. Li, X. Hou, and G. Liu, *Nanoscale* 5, 8375 (2013).
22. A.M. Quittet, M.I. Bell, M. Krauzman, and P.M. Raccah, *Phys. Rev. B* 14, 5068 (1976).
23. A. Bartasyte, J. Kreisel, W. Peng, and M. Guillouxviry, *Appl. Phys. Lett.* 96, 633 (2010).
24. J.A. Baier-Saip, E. Ramos-Moor, and A.L. Cabrera, *Solid State Commun.* 135, 367 (2005).
25. V.V. Atuchin, I.E. Kalabin, V.G. Kesler, and N.V. Pervukhina, *J. Electron. Spectrosc.* 142, 129 (2005).
26. R. Sawyer, H.W. Nesbitt, and R.A. Secco, *J. Non-Cryst. Solids.* 358, 290 (2012).
27. V.V. Atuchin, V.G. Kesler, N.Y. Maklakova, L.D. Pokrovsky, and V.N. Semenenko, *Surf. Interface Anal.* 34, 320 (2002).
28. B.J. Tan, K.J. Klabunde, and P.M.A. Sherwood, *J. Am. Chem. Soc.* 113, 855 (1991).
29. V.V. Atuchin, V.G. Kesler, V.K. Sapozhnikov, and V.N. Yakovenchuk, *Mater. Charact.* 59, 1329 (2008).
30. V.V. Atuchin, J.C. Grivel, A.S. Korotkov, and Z. Zhang, *J. Solid State Chem.* 181, 1285 (2008).
31. P. Pertosa and F.M. Michel-Calendini, *Phys. Rev. B.* 17, 2011 (1978).
32. T. Boningari, P.R. Ettireddy, A. Somogyvari, Y. Liu, A. Vorontsov, C.A. McDonald, and P.G. Smirniotis, *J. Catal.* 325, 145 (2015).
33. G. Shirane, H. Danner, A. Pavlovic, and R. Pepinsky, *Phys. Rev.* 93, 672 (1954).
34. Q. Wei, Z. Wang, X. Li, X. Long, and Z.G. Ye, *Chem. Mater.* 21, 506 (2009).
35. C. Long, C. Qi, W. Yun, W. He, Y. Li, and H. Fan, *J. Mater. Chem. C* 3, 8852 (2015).
36. W. Zhou, H. Deng, P. Yang, and J. Chu, *Appl. Phys. Lett.* 105, 134 (2014).
37. N. Masó and A.R. West, *Chem. Mater.* 27, 1552 (2015).
38. J. Wu, J. Wang, D. Xiao, and J. Zhu, *J. Appl. Phys.* 110, 064104 (2011).
39. T. He, K.D. Kreuer, Y.M. Baikov, and J. Maier, *Solid State Ionics* 95, 301 (1997).
40. A. Kazakopoulos, C. Sarafidis, K. Chrissafis, and O. Kalogirou, *Solid State Ionics* 179, 1980 (2008).
41. L. Ming, M.J. Pietrowski, R.A. De Souza, Z. Huairuo, I.M. Reaney, S.N. Cook, J.A. Kilner, and D.C. Sinclair, *Nat. Mater.* 13, 31 (2014).
42. Y. Sun, H. Liu, H. Hao, L. Zhang, and S. Zhang, *Ceram. Int.* 41, 931 (2015).
43. M. Coskun, O. Polat, F.M. Coskun, Z. Durmus, M. Caglar, and A. Turut, *Mater. Sci. Semicond. Proc.* 109, 104923 (2020).
44. M. Prades, H. Beltrán, E. Cordoncillo, P.J. Alonso, N. Masó, and A.R. West, *Phys. Status Solidi* 209, 2267 (2012).
45. D.S. Shang, Q. Wang, L.D. Chen, R. Dong, X.M. Li, and W.Q. Zhang, *Phys. Rev. B* 73, 245427 (2006).